North Pacific Decadal Variability and Climate Change in the IPCC AR4 Models

JASON C. FURTADO* AND EMANUELE DI LORENZO

School of Earth and Atmospheric Sciences, Georgia Institute of Technology, Atlanta, Georgia

NIKLAS SCHNEIDER

International Pacific Research Center, University of Hawaii at Manoa, Honolulu, Hawaii

NICHOLAS A. BOND

NOAA/Pacific Marine Environmental Laboratory, Seattle, Washington

(Manuscript received 17 December 2009, in final form 20 October 2010)

ABSTRACT

The two leading modes of North Pacific sea surface temperature (SST) and sea level pressure (SLP), as well as their connections to tropical variability, are explored in the 24 coupled climate models used in the Intergovernmental Panel on Climate Change (IPCC) Fourth Assessment Report (AR4) to evaluate North Pacific decadal variability (NPDV) in the past [twentieth century; climate of the twentieth century (20C3M) scenario] and future [twenty-first century; Special Report on Emissions Scenarios (SRES) A1B scenario] climate. Results indicate that the two dominant modes of North Pacific oceanic variability, the Pacific decadal oscillation (PDO) and the North Pacific Gyre Oscillation (NPGO), do not exhibit significant changes in their spatial and temporal characteristics under greenhouse warming. However, the ability of the models to capture the dynamics associated with the leading North Pacific oceanic modes, including their link to the corresponding atmospheric forcing patterns and to tropical variability, is questionable.

The temporal and spatial statistics of the North Pacific Ocean modes exhibit significant discrepancies from observations in their twentieth-century climate, most visibly for the second mode, which has significantly more low-frequency power and higher variance than in observations. The dynamical coupling between the North Pacific Ocean and atmosphere modes evident in the observations is very strong in the models for the first atmosphere–ocean coupled mode, which represents covariability of the PDO pattern with the Aleutian low (AL). However, the link for the second atmosphere–ocean coupled mode, describing covariability of an NPGO-like SST pattern with the North Pacific Oscillation (NPO), is not as clearly reproduced, with some models showing no relationship between the two.

Exploring the tropical Pacific–North Pacific teleconnections reveals more issues with the models. In contrast with observations, the atmospheric teleconnection excited by the El Niño–Southern Oscillation in the models does not project strongly on the AL–PDO coupled mode because of the displacement of the center of action of the AL in most models. Moreover, most models fail to show the observational connection between El Niño Modoki–central Pacific warming and NPO variability in the North Pacific. In fact, the atmospheric teleconnections associated with El Niño Modoki in some models have a significant projection on, and excite the AL–PDO coupled mode instead. Because of the known links between tropical Pacific variability and NPDV, these analyses demonstrate that focus on the North Pacific variability of climate models in isolation from tropical dynamics is likely to lead to an incomplete view, and inadequate prediction, of NPDV.

1. Introduction

North Pacific decadal variability (NPDV) is a key component in predictability studies of both regional and global climate change. Namias (1969) identified ''climatic regimes'' linked to changes in North Pacific sea surface temperature (SST) induced by shifts in atmospheric sea level pressure (SLP) patterns in both the

* Current affiliation: Atmospheric and Environmental Research, Inc., Lexington, MA.

Corresponding author address: Jason C. Furtado, Atmospheric and Environmental Research, Inc., 131 Hartwell Ave., Lexington, MA 01821.
E-mail: jfurtado@aer.com

DOI: 10.1175/2010JCLI3584.1

winter and summer. Subsequent studies by Namias (1972) and Davis (1976) explored the predictability aspect of these large-scale patterns of variability in the North Pacific in both the atmosphere and the ocean, the latter of which retains more memory and can thus sustain multidecadal variability. Though studies of NPDV remained dormant through the 1980s, the emergence of the El Niño–Southern Oscillation (ENSO) phenomenon in the climate literature in the 1990s reinvigorated interest in the subject (e.g., Trenberth 1990; Graham et al. 1994; Trenberth and Hurrell 1994; Zhang et al. 1997). The discovery of links between NPDV and changes in marine ecosystems (Mantua et al. 1997; Mantua and Hare 2000), along with its connections to tropical Pacific climate variability (e.g., Alexander et al. 2002; Anderson 2003; Newman et al. 2003; Deser et al. 2004; Newman 2007; Alexander et al. 2008; Di Lorenzo et al. 2008), emphasizes the need to better understand and characterize NPDV for global climate change predictions.

Two patterns of climate variability in the North Pacific generally characterize NPDV: the Pacific decadal oscillation (PDO; Mantua et al. 1997) and the recently identified North Pacific Gyre Oscillation (NPGO; Di Lorenzo et al. 2008). The PDO is defined as the leading empirical orthogonal function (EOF) of North Pacific SST anomalies (SSTa), and its positive phase is characterized by negative SSTa in the central North Pacific encircled by positive SSTa along the North American coastline. The PDO is linked to atmospheric variability in the Aleutian low (AL) and downstream changes in North American wintertime weather (e.g., Latif and Barnett 1996). Studies also link changes in the PDO to changes in marine ecosystems (e.g., Mantua et al. 1997; Yasuda et al. 1999; McGowan et al. 2003).

The second pattern of North Pacific climate variability, the NPGO, is formally defined as the second leading mode of northeast Pacific sea surface height (SSH) anomalies (Di Lorenzo et al. 2008). This pattern physically represents changes in the strength of the subtropical and subpolar gyres in the North Pacific and tracks prominent decadal fluctuations in salinity and nutrients observed in the central and eastern North Pacific (Di Lorenzo et al. 2009). Chhak et al. (2009) illustrated that the atmospheric forcing pattern of the NPGO is associated with the North Pacific Oscillation (NPO; e.g., Walker and Bliss 1932; Rogers 1981; Linkin and Nigam 2008), the second leading pattern of North Pacific SLP anomalies (SLPa). Ceballos et al. (2009) also linked the NPGO to changes in strength of the Kuroshio–Oyashio Extension current, therefore showing that NPGO variability latitudinally spans the North Pacific. The SSTa pattern associated with the NPGO is closely related to the second leading mode of North Pacific SSTa, referred to as the ''Victoria mode'' (Bond et al. 2003), and the second leading mode of Pacific-wide SSTa (Di Lorenzo et al. 2008). Recent evidence also suggests that the NPGO is a decadal-scale integrated response to low-frequency extratropical atmospheric forcing initiated by ''El Niño Modoki'' (Ashok et al. 2007) or central Pacific warming (CPW) (Di Lorenzo et al. 2010).

Given the links between the PDO and the NPGO and global climate, the predictability and characterization of these two modes in coupled climate models is an important open question in climate dynamics. Thus far, studies concerning long-term predictability of Pacific climate have focused on changes in the amplitude and frequency of ENSO and subsequent effects on teleconnection patterns (e.g., Meehl et al. 2006; Merryfield 2006; Yeh and Kirtman 2007). Overland and Wang (2007), by contrast, examined changes in the PDO under future warming scenarios in 10 coupled models used in the Intergovernmental Panel on Climate Change (IPCC) Fourth Assessment Report (AR4). This study found that the ensemble mean of the 10 models predicted uniform warming of the entire North Pacific basin with no change in the mean spatial pattern of the PDO. Newman (2007) explored interannual-to-decadal predictability of tropical and North Pacific SSTs in the IPCC models and concluded that North Pacific–tropical Pacific connections in the IPCC models were poorly represented, thus affecting predictability of decadal-scale variability with the models. Considering these previous studies, there still remains questions on potential changes in the frequency of the leading modes of North Pacific variability and the degree to which these modes of variability are tied to atmospheric forcing patterns, both directly and remotely.

This study addresses some of these outstanding issues through analysis of output from the 24 coupled climate models used in the IPCC AR4. The goals of the study are as follows: 1) to quantify the statistics of the leading patterns of NPDV climate variability, both in hindcast (twentieth century) simulations and future (twenty-first century) projections; 2) to evaluate the relationship between atmospheric forcing and the oceanic modes of NPDV; and 3) to assess the degree to which known atmospheric–oceanic teleconnections between the tropical Pacific and the North Pacific are represented in the models. Data and techniques used are first presented in section 2. Section 3 parallels Overland and Wang (2007) in looking at the leading EOFs of North Pacific SSTa as well as the power spectra associated with these leading patterns. Then, section 4 explores the use of a simple autoregressive model of order-1 (AR-1 model)

to evaluate atmosphere–ocean connections in the North Pacific. Section 5 explores how the models capture teleconnections between the tropical Pacific and the North Pacific associated with both the canonical ENSO and CPWs. A synthesis of the results and implications for future NPDV evaluation studies follow.

2. Data and methods

a. Observations

The low-frequency variability of the Pacific is investigated using observational analyses of SLP and SST. SLP data are taken from the National Centers for Environmental Prediction (NCEP)–National Center for Atmospheric Research (NCAR) Reanalysis Project (Kistler et al. 2001), while SST data are taken from the National Oceanic and Atmospheric Administration (NOAA) Extended Reconstruction SST dataset, version 3 (Smith et al. 2008). Both datasets contain monthly-mean values from 1950–2008 and are natively gridded onto a 2.5° × 2.5° latitude–longitude grid globally for SLP and a 2° × 2° grid for SST.

b. Model output

The source of the model outputs used in this study are the 24 coupled climate models that are part of the Coupled Model Intercomparison Project, phase 3 (CMIP3) and that were used for the IPCC AR4 (Table 1). The model output is available for downloading and processing through FTP or Open-Source Project for a Network Data Access Protocol (OPeNDAP) from the Program for Climate Model Diagnosis and Intercomparison (PCMDI) at the Lawrence Livermore National Laboratory (more information on the program is available at http://www-pcmdi.llnl.gov/). We use the climate of the twentieth century (20C3M) scenario (i.e., greenhouse gas concentrations increase throughout the twentieth century as in observations) to represent the twentieth-century climate and the Special Report on Emission Scenarios (SRES) A1B scenario (i.e., atmospheric carbon dioxide levels increase to 720 ppm by 2100 and are stabilized at that level thereafter) to represent the twenty-first-century climate.

Multiple realizations of the monthly-mean SLP and SST output are extracted for each model (see Table 1). All available realizations are used in processing the statistics for a particular model; that is, the mean value of statistics from all realizations of a particular model is used as the climate signature for that model. The incorporation of all realizations allows us to avoid run-to-run discrepancies in the models, as averaging will ''smooth'' the statistics. However, every model does not have the same number of realizations, so one disadvantage of this method is that models with only one realization available [e.g., the Bjerknes Centre for Climate Research (BCCR) Climate Model version 2 (BCM2)] may be affected more by noise than models with multiple realizations [e.g., the Goddard Institute for Space Studies Model E-R (GISS-ER)]. For 8 of the 24 models, only one realization for each scenario was available.

The spatial resolution for SLP and SST in the models varies between models and within the same model for atmospheric and oceanic variables. To facilitate comparisons with the observations, the SLP and SST fields are interpolated onto the same grids as their observational counterparts (i.e., 2.5° × 2.5° for SLP and 2° × 2° for SST). For analyses in the North Pacific, the spatial domain is defined as 15°–70°N in latitude and from 80°E to 65°W in longitude. For EOF analyses of the tropical Pacific only, the spatial domain is changed in latitude to 20°S–20°N. When exploring North Pacific and tropical Pacific connections together, we use the latitudinal domain 40°S–70°N. These same domains are used for observational analyses.

Temporally, output from model years 1900–99 represents twentieth-century climate, while model years 2001–2100 are used for the twenty-first century.[1] Though the model analyses span a longer period of time than the observations, the leading modes of SSTa and SLPa variability in space are generally insensitive to whether the same time periods are chosen or not. Thus, our analyses and conclusions are not greatly affected by this difference in time.

c. Statistical techniques

The primary statistical techniques used to isolate patterns of climate variability in the Pacific are traditional EOF and combined EOF (cEOF) analysis of the SLPa and SSTa fields. Traditional EOF analysis aims to break a large dataset with many state vectors, represented by **A**, into a smaller set of state vectors that explains a large fraction of the variability in the original dataset. With cEOF analysis, two or more variables are placed into **A**, which is subsequently decomposed using singular value decomposition (SVD; e.g., Bretherton et al. 1992). Hence, the resulting matrices depict shared patterns of variability among several variables.

For EOF analysis, each field is weighted by the square root of the cosine of latitude before computing the

[1] The time span for the models in each scenario is different. Some models include the year 2000 in the 20C3M scenario, while others include the year 2000 in the SRES A1B scenario. For that reason, the year 2000 is excluded from the analysis.

TABLE 1. List of models from the IPCC AR4 analyzed in this study, along with the number of realizations available for processing for both the 20C3M and SRES A1B scenarios. Abbreviations used are as follows: Commonwealth Scientific and Research Organization (CSIRO); National Oceanic and Atmospheric Administration (NOAA); National Aeronautics and Space Administration (NASA).

Originating Group, Country	Model name	Realizations (20C3M/SRES A1B)
Bjerknes Centre for Climate Research, Norway	BCCR-BCM2.0	1/1
Canadian Centre for Climate Modeling and Analysis, Canada	CGCM3.1 (T47)	5/5
Canadian Centre for Climate Modeling and Analysis, Canada	CGCM3.1 (T63)	1/1
Météo-France/Centre National de Recherches Météorologiques, France	CNRM-CM3	1/1
CSIRO Atmospheric Research, Australia	CSIRO3.0	3/1
CSIRO Atmospheric Research, Australia	CSIRO3.5	1/1
NOAA Geophysical Fluid Dynamics Laboratory, United States of America	GFDL CM2.0	3/1
NOAA Geophysical Fluid Dynamics Laboratory, United States of America	GFDL CM2.1	3/1
NASA Goddard Institute for Space Studies, United States of America	GISS-AOM	2/2
NASA Goddard Institute for Space Studies, United States of America	GISS-EH	5/3
NASA Goddard Institute for Space Studies, United States of America	GISS-ER	9/5
Institute of Atmospheric Physics, China	IAP FGOALS-g1.0	3/3
Instituto Nazionale di Geofisica e Vulcanologia (INGV) and Max Planck Institute for Meteorology, Italy/Germany	INGV ECHAM4	1/1
Institute of Numerical Mathematics, Russia	INM-CM3.0	1/1
Institute Pierre Simon Laplace (IPSL), France	IPSL Coupled Model, version 4 (CM4)	1/1
Center for Climate System Research, Japan	MIROC(hires)	1/1
Center for Climate System Research, Japan	MIROC(medres)	3/3
Meteorological Institute of the University of Bonn and Meteorological Research Institute of KMA, Germany/Korea	MIUBECHOG	5/3
Max Planck Institute for Meteorology, Germany	MPI ECHAM5	4/4
Meteorological Research Institute, Japan	MRI CGCM2.3.2	5/5
National Center for Atmospheric Research, United States of America	NCAR CCSM3.0	8/7
National Center for Atmospheric Research, United States of America	NCAR PCM1	4/4
Hadley Centre for Climate Prediction and Research/Met Office, United Kingdom	UKMO HadCM3	2/1
Hadley Centre for Climate Prediction and Research/Met Office, United Kingdom	UKMO HadGEM1	2/1

eigenvalues and eigenfunctions of **A**. For cEOF analysis, SLPa and SSTa are used to construct **A**. Because the two fields have different variances and magnitudes, each field is normalized separately before applying SVD. The SLPa field is first normalized by the standard deviation at each latitude to account for the greater variance in SLP in the extratropics. Then, both fields are standardized by the mean standard deviation in the respective field before SVD analysis is performed. Only the two leading patterns of climate covariability are retained, as these two patterns pass the significance test of North et al. (1982) and are also of most interest for our study on NPDV.

For both EOF and cEOF analyses, the anomaly fields are calculated by removing the climatological monthly mean from the raw fields. The anomalies are then linearly detrended, and a 3-month temporal filter is applied before eigenanalysis. Furthermore, we retain only the December, January, and February (DJF) values of the filtered fields. The choice of using winter values only versus the entire year was made because the North Pacific atmosphere–ocean connections are dominant in the boreal winter months. Expansion coefficient (EC) time series are obtained by projecting individual *unfiltered* monthly-mean anomaly maps onto the corresponding EOF–cEOF spatial pattern for each mode. These time series are then used for all temporal analyses. Table 2 provides a list of the nomenclature used to refer to the various EOFs, cEOFs, and EC time series presented in this paper.

To explore the temporal variability of the leading SLPa and SSTa patterns, spectral analysis is used. All power spectra are normalized so that the area under the individual spectrum is unity. Hence, the values represented in the power spectra are the percentage of total variance explained at that frequency. Periods with significant power are determined using the method outlined in Torrence and Compo (1998)—a mean normalized red-noise spectrum is calculated for the particular index, and the 95% confidence spectrum is then

TABLE 2. Abbreviations for various EOF and cEOF patterns and EC time series used in this paper.

Abbreviation	Description
$EOF\text{-}1_{SST}/EOF\text{-}1_{SLP}$	The spatial representation of the leading mode of variability of North Pacific boreal winter SSTa/SLPa.
$EOF\text{-}2_{SST}/EOF\text{-}2_{SLP}$	The spatial representation of the second leading mode of variability of North Pacific boreal winter SSTa/SLPa.
$cEOF\text{-}1_{SST}/cEOF\text{-}1_{SLP}$	The spatial representation in SSTa/SLPa space of the leading mode of covariability between North Pacific boreal winter SSTa and SLPa.
$cEOF\text{-}2_{SST}/EOF\text{-}2_{SLP}$	The spatial representation in SSTa/SLPa space of the second leading mode of covariability between North Pacific boreal winter SSTa and SLPa.
$EOF\text{-}l_{tropics\text{-}SST}/EOF\text{-}2_{tropics\text{-}SST}$	The leading/second leading mode of variability of tropical Pacific boreal winter SSTa.
$EC\text{-}1_{SST}/EC\text{-}1_{SLP}$	The monthly expansion coefficient time series associated with $EOF\text{-}1_{SST}/EOF\text{-}1_{SLP}$.
$EC\text{-}2_{SST}/EC\text{-}2_{SLP}$	The monthly expansion coefficient time series associated with $EOF\text{-}2_{SST}/EOF\text{-}2_{SLP}$.
$cEC\text{-}1_{SST}/cEC\text{-}1_{SLP}$	The monthly expansion coefficient time series associated with $cEOF\text{-}1_{SST}/cEOF\text{-}1_{SLP}$.
$cEC\text{-}2_{SST}/cEC\text{-}2_{SLP}$	The monthly expansion coefficient time series associated with $cEOF\text{-}2_{SST}/cEOF\text{-}2_{SLP}$.
$EC\text{-}l_{tropics\text{-}SST}/EC\text{-}2_{tropics\text{-}SST}$	The monthly expansion coefficient time series associated with $EOF\text{-}l_{tropics\text{-}SST}/EOF\text{-}2_{tropics\text{-}SST}$.

found by multiplying the red noise spectrum by the appropriate F statistic. Only peaks exceeding the value of the significance spectrum as a function of period are then plotted. Significance testing for changes in variance of the power spectra between the 20C3M and SRES A1B scenarios uses the F statistic.

Significance testing for correlations in time and space is done through a Monte Carlo approach. Two-thousand red-noise time series with the same lag-1 correlation coefficient of each series are simulated, and the probability density function (PDF) of the cross correlation between those simulated series is computed. Desired significance levels are found by computing the area under the PDF and comparing those values to the cross correlation between our two time series to accept or reject the null hypothesis.

Finally, the ensemble-mean statistics for the models are computed as the mean of the individual statistic being analyzed. For example, the ensemble-mean leading pattern of variability of North Pacific SSTa is calculated as follows: 1) the leading EOF is computed for each model, and then the SSTa from the model are regressed onto the standardized first principal component time series; 2) the sign of the anomalies are changed such that the sign of one of the poles in the pattern matches among the models; and 3) the individual regression maps are averaged together. Similarly, for power spectra, the individual normalized power spectra of the models are averaged together to get the power spectrum of the ensemble mean of the models.

3. Leading modes of North Pacific SSTa in present and future climate

The study begins by extending the statistical analysis of Overland and Wang (2007), who explored changes of the first leading mode of North Pacific SSTa (i.e., the PDO) in the IPCC models, to also include the second leading mode. Figure 1 compares the two leading modes ($EOF\text{-}1_{SST}$ and $EOF\text{-}2_{SST}$) from observations (Figs. la and 1b) to the mean EOF patterns from the models (Figs. lc and 1d). In the observations, the canonical PDO pattern emerges in $EOF\text{-}1_{SST}$ (Fig. 1a), with negative central North Pacific SSTa encircled by positive SSTa to the east. The temporal evolution of the first mode ($EC\text{-}1_{SST}$) closely tracks the monthly PDO index (downloaded from http://jisao.washington.edu/pdo/PDO.latest); the correlation between the two time series is $r = 0.71$ ($p < 0.01$). The second leading pattern of SSTa (Fig. lb) exhibits a northeast–southwest-oriented tripole, which is very similar to the SSTa regression pattern associated with the NPGO index and that of the Victoria Mode (Bond et al. 2003). The correlation between the temporal evolution of the second mode ($EC\text{-}2_{SST}$) and the monthly NPGO index (downloaded from http://ocean.eas.gatech.edu/npgo) is $r = 0.28$ ($p < 0.05$). The ensemble-mean $EOF\text{-}1_{SST}$ (Fig. lc) compares visually well with the observations, while there are two main differences for $EOF\text{-}2_{SST}$ (Fig. 1d): the lack of the tripole structure and the placement of the positive anomaly closer to the North American coast compared to observations (Figs. lb and 1d).

Spatial correlations between individual model patterns of $EOF\text{-}1_{SST}$ and $EOF\text{-}2_{SST}$ and the observational counterparts are shown in Fig. 2. All shaded correlations exceed the 95% significance level. For $EOF\text{-}1_{SST}$ and $EOF\text{-}2_{SST}$ the spatial correlations for the ensemble-mean patterns are $r = 0.76$ and $r = 0.81$, respectively. Note that spatial correlations vary considerably among individual models, with some [e.g., the Meteorological Institute of the University of Bonn, ECHO-G Model (MIUBECHOG) and NCAR Community Climate System Model, version 3 (CCSM3)] having lower spatial correlations for both North Pacific SST EOFs than the

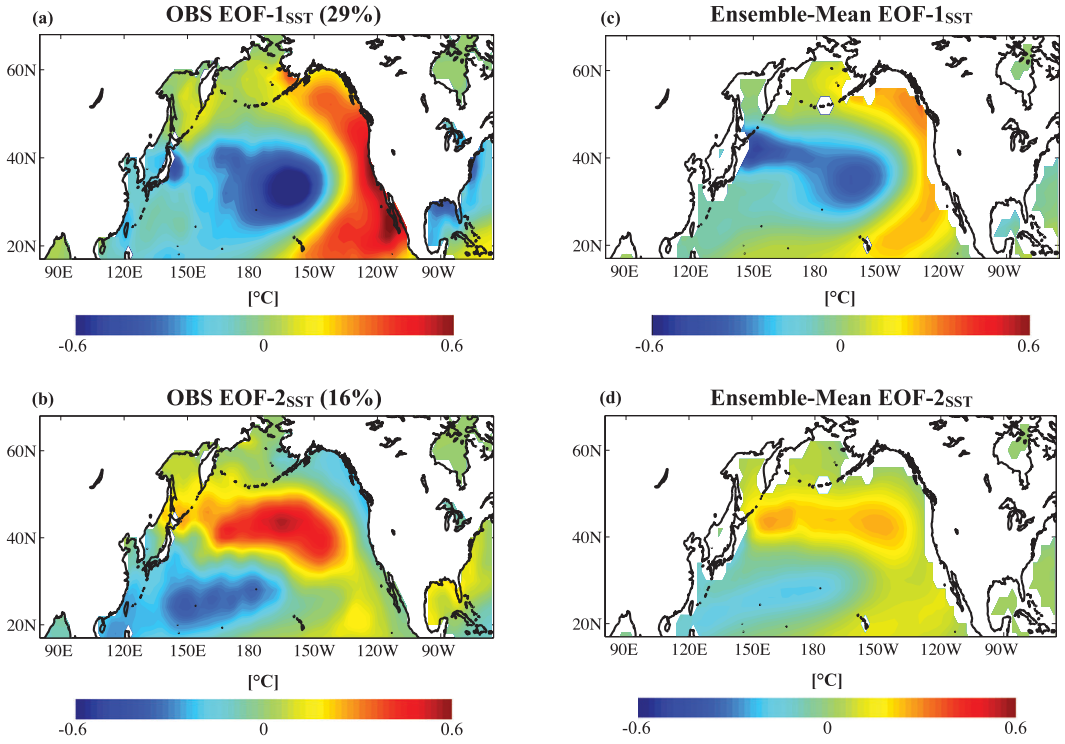

FIG. 1. (a) Regression of observed DJF SSTa (°C) onto the standardized first principal component time series of observed North Pacific DJF SSTa. Percent variance explained by the mode is given in the title. (b) As in (a), but using the standardized second principal component time series of North Pacific DJF SSTa. (c) The mean of the regression patterns of model DJF SSTa onto the standardized first principal component time series of model DJF North Pacific SSTa (i.e., the ensemble-mean pattern). (d) As in (c), but for the standardized second principal component time series of North Pacific DJF SSTa.

ensemble mean, while others [e.g., both Model for Interdisciplinary Research on Climate (MIROC) models] have higher correlations than the ensemble mean.

The spatial patterns of EOF-1_{SST} and EOF-2_{SST} remain virtually unchanged for the future with significant spatial correlations between the ensemble mean and the observations (not shown). Individual model spatial correlations differ between the 20C3M and SRES A1B scenarios but not significantly, suggesting that spatially the leading patterns of North Pacific SSTa are statistically stationary.

Figure 3 presents the power spectra for the two leading patterns of North Pacific SSTa. The ensemble-mean power spectrum of the models for the EC-1_{SST} index closely resembles that of the observations for the twentieth century (Fig. 3a). Almost all models exhibit power in the decadal (10–20 years) band, although to varying degrees. The BCCR-BCM2.0, the Geophysical Fluid Dynamics Laboratory Climate Model version 2.0 (GFDL CM2.0), and the GISS Model E-H (GISS-EH) have the strongest power in the decadal bands, while the Commonwealth Scientific and Industrial Research Organisation Mark version 3.5 (CSIRO3.5) and the NCAR–PCM1 models exhibit weaker decadal-scale power. For the second mode (EC-2_{SST}; Fig. 3b), the results are less consistent with observations. The observed EC-2_{SST} power spectrum has a generally weak, broad spectrum with two significant peaks—one at 7–12 years and the other at 4–5 years. The ensemble-mean power spectrum, by contrast, has its maximum power in the 15–20-yr band with decreasing power toward higher frequencies. Individual model members follow the characteristics of the ensemble-mean power spectrum except for the GFDL CM2.1, which captures the interannual peak seen in observations. Differences in power spectra between the 20C3M and SRES A1B scenarios for the EC-1_{SST} and EC-2_{SST} indices are insignificant in nearly every model (not shown). Only two models (the BCCR-BCM2.0 and the GISS-EH) predict significant increases power at higher frequencies (2–5 years) for both leading modes; however, since these models have low spatial correlations with observations (Fig. 2), we discount these results.

We also examine how much of the total variance is explained by the two leading modes of the models compared to observations. Table 3 presents the variance of the model EC-1_{SST} and EC-2_{SST} indices (columns 2

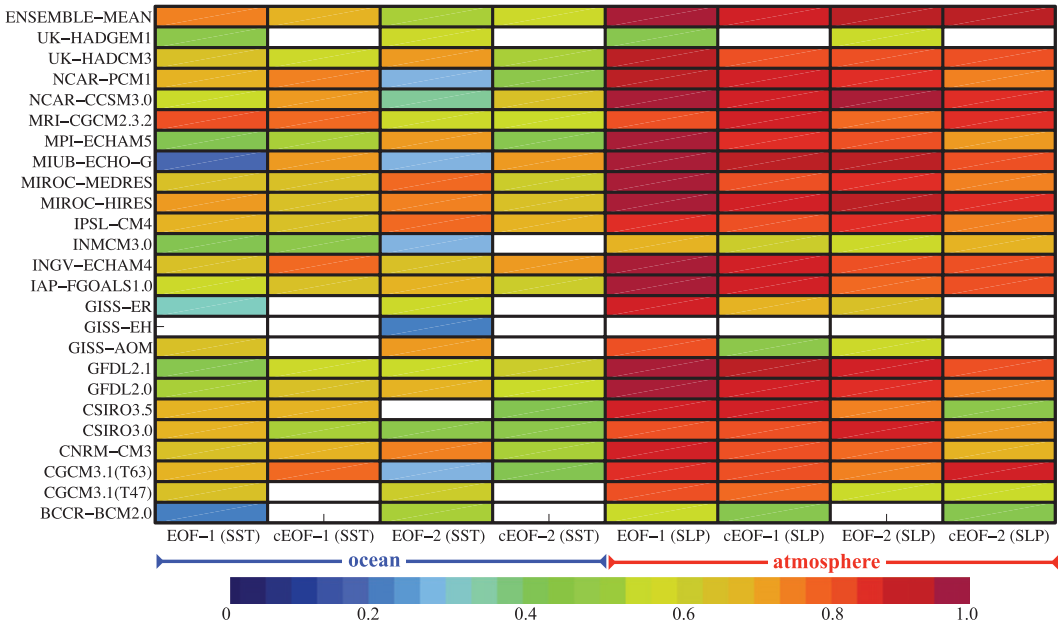

FIG. 2. Spatial correlations of the leading EOFs and cEOFs of North Pacific wintertime SLP and SST between the 20C3M runs of the models and observations. Only spatial correlations exceeding the 95% significance level are shaded.

and 3), normalized by the variance of the observed index, for both the 20C3M and SRES A1B scenarios. This normalization facilitates comparison among the models and also between the 20C3M and SRES A1B scenarios. For the EC-1_{SST} index in the 20C3M output, most of the models have much smaller variance than the observed index, with the GISS Atmosphere–Ocean Model (GISS-AOM), the GISS-ER, and the MIROC high resolution [MIROC(hires)] having variances less than 10% of the observed index (Table 3, column 2). Only two models have variances for the EC-1_{SST} index greater than observed [the Institute of Numerical Mathematics Coupled Model, version 3.0 (INM-CM3.0) and NCAR–PCM1). By contrast, for the 20C3M EC-2_{SST} index (Table 3, Column 3), every model except for three [again, the GISS-AOM, GISS-ER, and MIROC(hires)] has a variance in its index larger than that in observations, ranging from double (e.g., the NCAR CCSM3.0 model) to nearly 12 times the observed variance (the MIUBECHOG model). When looking at differences between the 20C3M and SRES A1B scenarios, we find no consensus in the direction of change in variance of either index among the models, though the ensemble mean suggests a decrease in variance for both indices.

4. Relations between North Pacific atmospheric and oceanic variability

The leading modes of North Pacific SSTa variability are a combination of both intrinsic variability in the ocean and a response to external forcing by the overlying extratropical atmosphere (e.g., Pierce et al. 2001; Miller et al. 2004; Chhak et al. 2009). For coupled climate models to capture NPDV accurately, we should expect that similar covariances and ocean–atmosphere dynamical links exist in the models. This section offers tests for the covariability between SLPa and SSTa in the North Pacific and an AR-1 model to evaluate the degree of forcing the North Pacific atmospheric circulation contributes to the forcing of the dominant modes of oceanic variability in the region.

a. Leading modes of North Pacific SLPa in the IPCC models

Before performing an analysis of the coupled ocean–atmosphere modes of variability in the North Pacific, we compare the leading patterns of atmospheric variability in the SLPa fields for each model to observations. We find that the spatial correlations of the leading two North Pacific SLP EOFs in the models versus the observations are high and significant (Fig. 2) and typically higher than the North Pacific SST EOFs. The power spectra of the leading two SLP EOFs in the models compare well with the observations with a broad range of low power for low and high frequencies. There is no statistically significant difference between the ensemble mean and observed power spectrum for either the EC-1_{SLP} or EC-2_{SLP} index (not shown).

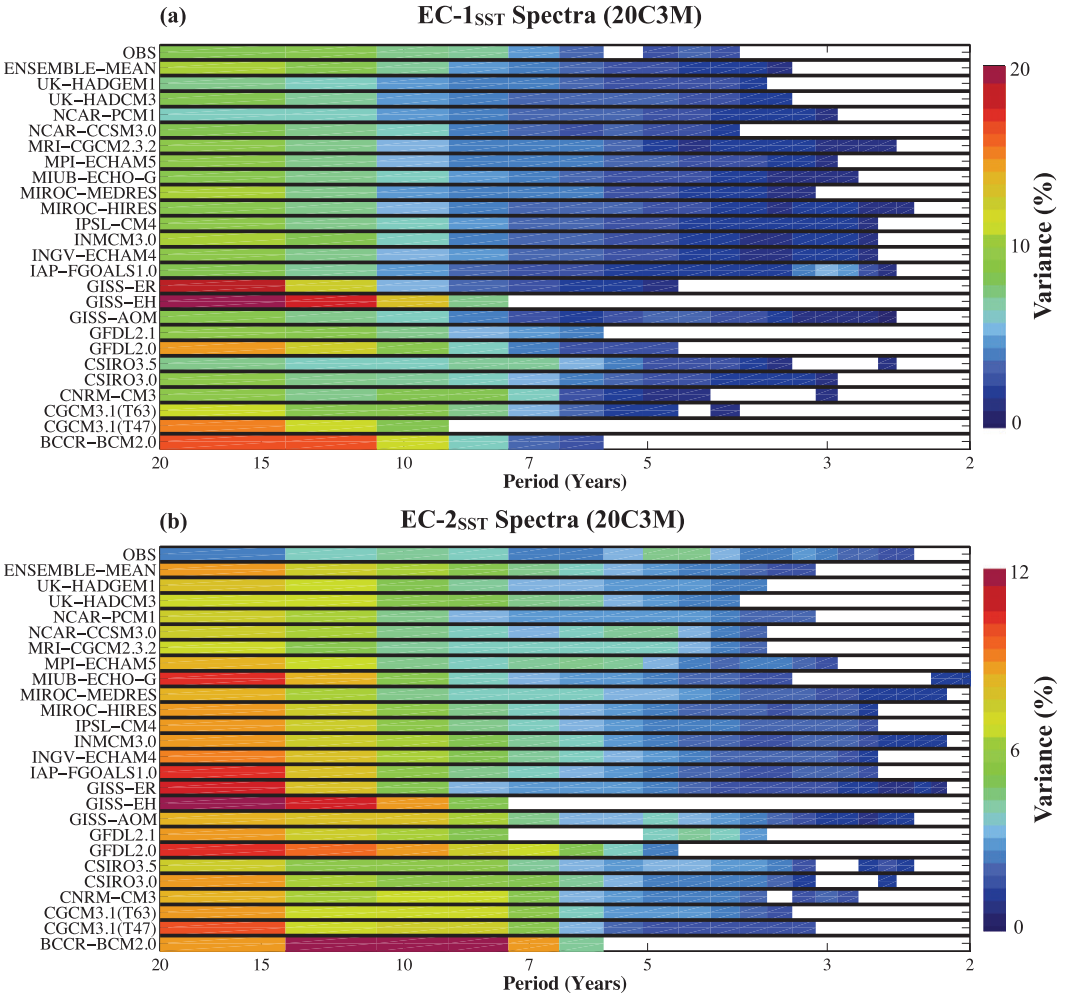

FIG. 3. (a) Power spectra (% of total variance explained) of the EC-1_{SST} index as a function of period (yr) for observations, the ensemble-mean of the models, and the 20C3M runs of the IPCC models. (b) As in (a), but for the EC-2_{SST} index. Only significant power values ($p < 0.05$) are shaded (see text for details on significance testing).

b. Coupled patterns of variability in the North Pacific Ocean and atmosphere

Figure 4 displays the two leading cEOF patterns between North Pacific SLPa and SSTa in observations during boreal winter. Together, the first two patterns explain 38% of the covariability in the two variables. The first pattern is dominated by a broad area of negative SLPa in the central and eastern North Pacific basin (Fig. 4a). This loading center resides to the south and east of the climatological center of the AL. The corresponding SSTa pattern (Fig. 4b) resembles the positive phase of the PDO displayed in Fig. la ($r = 0.98$; $p < 0.01$). Moreover, the cEC-1_{SST} and EC-1_{SST} indices are correlated at $r = 0.99$ ($p < 0.01$). For cEOF-2, the SLPa pattern (Fig. 4c) shows a distinct dipole, with centers of opposing sign over the Aleutian Islands and just north of Hawaii, representing the NPO (Walker and Bliss 1932; Rogers 1981; Linkin and Nigam 2008). The covarying SSTa pattern (Fig. 4d) portrays cold anomalies stretching from the southwestern North Pacific toward the northeast, surrounded by warm anomalies extending from the Kamchatka Peninsula southeastward toward North America and around to Hawaii. The spatial pattern is highly similar to that in Fig. lb ($r = 0.89$; $p < 0.01$), although there is a notable difference in the magnitude of the positive anomaly in the northernmost Pacific and in the positive anomalies in the subtropical North Pacific. When the spatial pattern in Fig. 4d is compared to the NPGO SSTa regression pattern, the spatial correlation is $r = 0.76$ ($p < 0.01$). Moreover, the cEC-2_{SST} index is significantly correlated with the EC-2_{SST} index ($r = 0.88$; $p < 0.01$) and the NPGO index ($r = 0.60$; $p < 0.01$).

When performing the same cEOF analysis on the 20C3M model output, we find substantial differences in the SLPa and SSTa fields in the two leading cEOF

TABLE 3. Normalized variance (i.e., actual variance divided by the variance of the same index in observations; dimensionless) of the EC-1_{SST} and EC-2_{SST} indices. Variance shown for both scenarios (20C3M/SRES A1B).

Model Name (data)	VAR (EC-1_{SST})	VAR (EC-2_{SST})
BCCR-BCM2.0	0.69/0.34	3.65/2.33
CGCM3.1 (T47)	0.19/0.14	1.55/1.01
CGCM3.1 (T63)	0.25/0.18	1.17/0.78
CNRM-CM3	0.70/0.58	3.52/4.29
CSIRO3.0	0.10/0.11	1.22/1.74
CSIRO3.5	0.25/0.08	1.41/1.81
GFDL CM2.0	0.63/1.25	6.50/4.72
GFDL CM2.1	0.38/0.14	6.07/1.14
GISS-AOM	0.02/0.04	0.40/0.49
GISS-EH	0.54/0.29	5.07/3.28
GISS-ER	0.05/0.09	0.55/0.74
IAP FGOALS-g1.0	1.00/0.56	8.95/2.89
INGV ECHAM4	0.21/0.04	2.29/0.20
INM-CM3.0	1.83/0.97	7.42/6.78
IPSL CM4	0.33/0.15	1.32/2.07
MIROC(hires)	0.08/0.11	0.70/1.11
MIROC(medres)	0.13/0.26	1.27/2.37
MIUBECHOG	0.82/0.53	11.94/9.36
MPI ECHAM5	0.66/0.69	7.43/7.00
MRI CGCM2.3.2	0.87/0.81	4.12/3.37
NCAR CCSM3.0	0.58/0.67	2.08/2.45
NCAR PCM1	1.37/1.03	8.10/5.51
UKMO HadCM3	0.55/0.77	4.56/2.27
UKMO HadGEM1	0.35/0.27	4.16/5.34
Ensemble mean	0.53/0.42	3.98/3.04
Observations	1.00	1.00

patterns (Fig. 5). The ensemble-mean patterns of SST and SLP for cEOF-1 (Figs. 5a and 5b) resemble overall those of the observations (spatial correlations shown in Fig. 2), albeit with two major differences: 1) the representation of the AL is oriented more zonally in the ensemble-mean pattern and encompasses most of the North Pacific basin with its center of action displaced toward the west; and 2) the SSTa pattern displays an elongated southwest–northeast negative pole, unlike the concentrated negative pole prominent in the observations (Fig. 4b). For cEOF-2, the SLPa pattern (Fig. 5c) is significantly correlated with the observations (r = 0.90) with the typical dipole structure of the NPO. In the SSTa field (Fig. 5d), the ensemble-mean SSTa pattern of cEOF-2 displays a weak tripole, and the positive anomalies do not extend into the eastern subtropical Pacific as in the observations. The spatial correlation between the ensemble-mean EOF-1_{SST} (EOF-2_{SST}) and cEOF-1_{SST} (cEOF-2_{SST}) is r = 0.78 (r = 0.59), which is significant at the 99% (95%) level.

When comparing cEOF-1_{SST} and cEOF-2_{SST} from each model with observations (Fig. 2) we generally find weaker correlations than the ones obtained by comparing the SST patterns inferred from the traditional EOF analysis. Six of the 24 models display insignificant spatial correlations for both cEOF-1_{SST} and cEOF-2_{SST} (Fig. 2). For the atmospheric cEOF patterns, spatial correlations are generally higher than the oceanic cEOF patterns, though four models have insignificant spatial correlations for cEOF-2_{SLP} (Fig. 2, column 8). As with the North Pacific SSTa EOFs, the cEOF patterns in both SLPa and SSTa remain unchanged spatially when examining the SRES A1B output.

c. *Reconstructing the* cEC-1_{SST} *and* cEC-2_{SST} *indices using a simple AR-1 model*

The atmospheric patterns depicted in the cEOF analyses are also dynamically linked to the leading modes of North Pacific SSTa variability. Latif and Barnett (1996) and Pierce et al. (2001) suggested that the leading pattern of North Pacific SSTa variability (i.e., the PDO) is forced through stochastic atmospheric forcing, primarily that due to the AL. Chhak et al. (2009) used output from an ocean model to illustrate that NPGO variability is forced, at least in part, by variability in the NPO. Given the similarities between the PDO/cEOF-1_{SST} and the NPGO/cEOF-2_{SST} in observations, we employ a simple AR-1 model to check for consistency between the atmospheric forcing patterns and North Pacific SSTa variability. This test solely explores the degree to which the atmospheric forcing patterns are connected to the underlying covariability SSTa patterns in both the observations and models. The AR-1 model equations are

$$\frac{d(\text{cEC-1}_{\text{SST-rec}})}{dt} = \beta_{\text{cEC-1}}\text{AL}(t) - \frac{\text{cEC-1}_{\text{SST-rec}}(t)}{\tau_{\text{cEC-1}}} + \varepsilon_1(t), \quad \text{and} \tag{1}$$

$$\frac{d(\text{cEC-2}_{\text{SST-rec}})}{dt} = \beta_{\text{cEC-2}}\text{NPO}(t) - \frac{\text{cEC-2}_{\text{SST-rec}}(t)}{\tau_{\text{cEC-2}}} + \varepsilon_2(t), \tag{2}$$

where AL(t) and NPO(t) are defined as the cEC-1_{SLP} and cEC-2_{SLP} time series, respectively, $\varepsilon(t)$ represents error/noise in the AR-1 model, and the subscript "rec" indicates that the indices are the reconstructed versions of the original indices. The coefficients ($\tau_{\text{cEC-1}}$, $\tau_{\text{cEC-2}}$, $\beta_{\text{cEC-1}}$, and $\beta_{\text{cEC-2}}$) are determined using least squares fitting. A simple Euler forward time step scheme is used in solving (1) and (2).

Figures 6 and 7 show the results of the AR-1 model for the cEC-1_{SST} (Fig. 6) and cEC-2_{SST} (Fig. 7) indices. In observations, the results indicate that AL variability accounts for about 32% of the variance of the cEC-1_{SST}

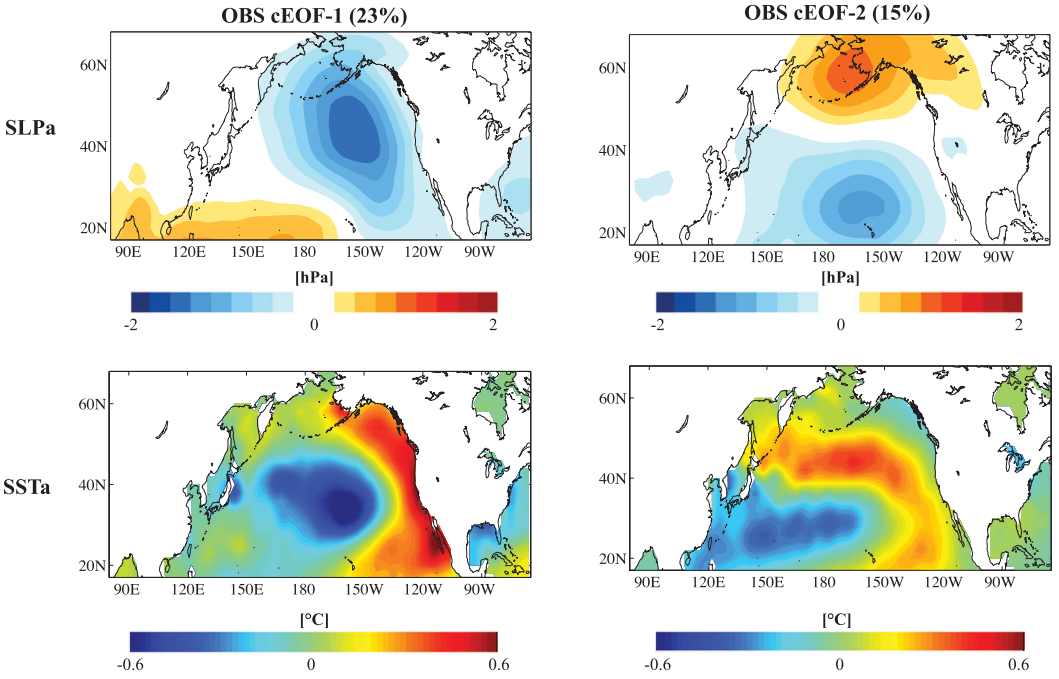

FIG. 4. Regression of observed DJF (a) SLPa (hPa) and (b) SSTa (°C) onto the standardized first principal component time series of the combined EOF analysis of North Pacific DJF SLPa–SSTa. Percent covariance explained by the mode is given in the title. (c) As in (a), but using the standardized second principal component time series of the combined EOF analysis of North Pacific DJF SLPa–SSTa. (d) As in (b), but using the standardized second principal component times series of the combined EOF analysis of North Pacific DJF SLPa–SSTa.

index (Fig. 6a), while NPO variability contributes to about 40% of the variance of the cEC-2_{SST} index (Fig. 7a). For the cEC-1_{SST} index in the models (Fig. 6b), every model but one [the Canadian Centre for Climate Modelling and Analysis Coupled General Circulation Model, version 3.1 (CGCM3.1) (T47), $r = 0.14$] shows significant ($p < 0.05$) correlations between their cEC-1_{SST} and cEC-$1_{SST\text{-}rec}$ indices. Significant correlation values range from $r = 0.63$ for the Max Planck Institute (MPI) ECHAM5 model to $r = 0.88$ for the Meteorological Research Institute Coupled General Circulation Model, version 2.3.2 (MRI CGCM2.3.2). The ensemble-mean correlation for the reconstruction of the cEC-1_{SST} index with the AR-1 model is $r = 0.75$ or 56% of total variance explained.

For the cEC-2_{SST} index (Fig. 7b), less reproducibility exists. Seven of the 24 models [the BCCR-BCM2.0, CGCM3.1 (T47), CGCM3.1 (T63), GISS-EH, Institute of Atmospheric Physics (IAP) Flexible Global Ocean–Atmosphere–Land System Model gridpoint version 1.0 (FGOALS-g1.0), INMCM3.0, and NCAR-CCSM3.0] have small, insignificant correlations. The remaining models show significant ($p < 0.05$) correlations ranging from $r = 0.24$ for the Centre National de Recherches Météorologiques Coupled Global Climate Model, version 3 (CNRM-CM3) to $r = 0.74$ for the MIROC(hires) model. The mean correlation among all models for the reconstruction of the cEC-2_{SST} index is $r = 0.47$, or 22% of total variance explained, which is considerably lower than the correlation derived from observations ($r = 0.63$ or 40% of variance explained). This result suggests that cEOF-2_{SST} is less consistent with direct atmospheric forcing by the NPO in the models than what is observed.

Table 4 shows the τ values derived for the AR-1 model results. For the cEC-1_{SST} index, $\tau_{cEC\text{-}1}$ values for all of the models except for the CGCM3.1 (T47) model are smaller than that seen in observations (10.2 months), with the ensemble-mean $\tau_{cEC\text{-}1}$ equal to 6.2 months. The lower-than-observed $\tau_{cEC\text{-}1}$ values suggest that the SST in the coupled models exhibit less memory in their leading mode of North Pacific SSTa, allowing more of the high-frequency atmospheric forcing (i.e., the AL) to contribute and drive the oceanic signal. For the cEC-2_{SST} reconstruction, the ensemble-mean value for $\tau_{cEC\text{-}2}$ is 8.8 months, which is larger than that from observations (5.8 months). For individual models, the six models with the largest values of $\tau_{cEC\text{-}2}$ are also those models with insignificant correlations in the AR-1 model test (Fig. 7b). This suggests that these coupled models generally exhibit more memory in the second covariability climate pattern in SSTa and have less dependence on high frequency NPO forcing. This conclusion is also supported by Fig. 3b—recall that the maximum power for the models

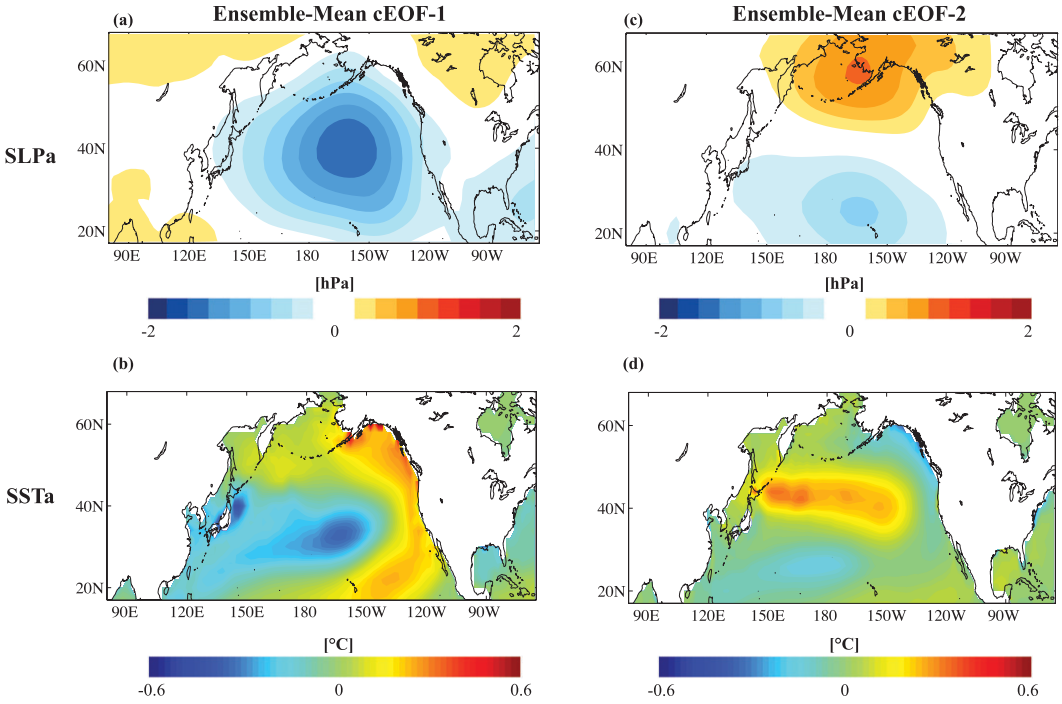

FIG. 5. The ensemble-mean leading pattern of covariability obtained through averaging individual regression maps of the model North Pacific DJF (a) SLPa (hPa) and (b) SSTa (°C) fields from the standardized first principal component time series of the combined EOF of North Pacific DJF SLPa–SSTa. (c) As in (a), but using the standardized second principal component time series of the combined EOF analysis of North Pacific DJF SLPa–SSTa. (d) As in (b), but using the standardized second principal component times series of the combined EOF analysis of North Pacific DJF SLPa–SSTa. Results are shown for the 20C3M runs.

is generally concentrated at periods greater than 10 years, unlike the "double peak" at decadal and interannual time scales in the observed spectrum.

Studies of North Pacific SST variability have identified reemergence as a significant component contributing to NPDV (e.g., Alexander et al. 1999; Deser et al. 2003). Indeed, the presence of reemergence means that North Pacific SST variability in general cannot be modeled entirely as an AR-1 process, but the leading modes and coupled modes of variability may still contain a significant component related to an AR-1 process. For example, in using the same AR-1 model as (1) but using the EC-1_{SLP} time series as the forcing, $\beta = 1$, and $\tau = 5$ months (i.e., the decorrelation time scale for the PDO index), the correlation between the actual PDO index (downloaded from http://jisao.washington.edu/pdo/PDO.latest) and the reconstruction is $r = 0.64$, which is significant at the 99% level. Thus, nearly 41% of the variability in the PDO index can be captured with the simple AR-1 model using AL variability as forcing. To test if the assumption of an AR-1 process is consistent with the cECs, Fig. 8 presents the winter-to-winter autocorrelation functions (ACFs) for the cEC-1_{SST} (Fig. 8a) and cEC-2_{SST} indices (Fig. 8b) for the observations (red line), the individual models (gray lines), and the ensemble-mean ACF (black line). For the models, there is a lot of spread amongst the ACFs (Fig. 8a, gray lines), though most of the models appear to have a simple exponential decay in their ACFs. For the observed cEC-1_{SST} index, the decay in the ACF over time is punctuated by brief "bumps" at lags of 5 and 10 years, which fall within the model ACF spread and are not statistically significant according to a Monte Carlo test. Some of the model ACFs exhibit some signature of longer-term memory, but the ensemble-mean cEC-1_{SST} ACF (Fig. 8a, black line) displays a strictly exponential decay, which offers evidence that the AR-1 modeling approach is adequate to explore the relationship between the atmospheric forcing and oceanic response in the cECs.

The ACFs for the cEC-2_{SST} index (Fig. 8b) indicate some consistency with our previous observation of longer-term memory of the second leading SST covariability pattern in the models. Note that for short lags (less than 4 years), the ensemble-mean ACF of the cEC-2_{SST} index generally has a slower rate of decay than the observed (black line compared to the red line in Fig. 8b). These higher correlations in the ensemble-mean ACF do indicate

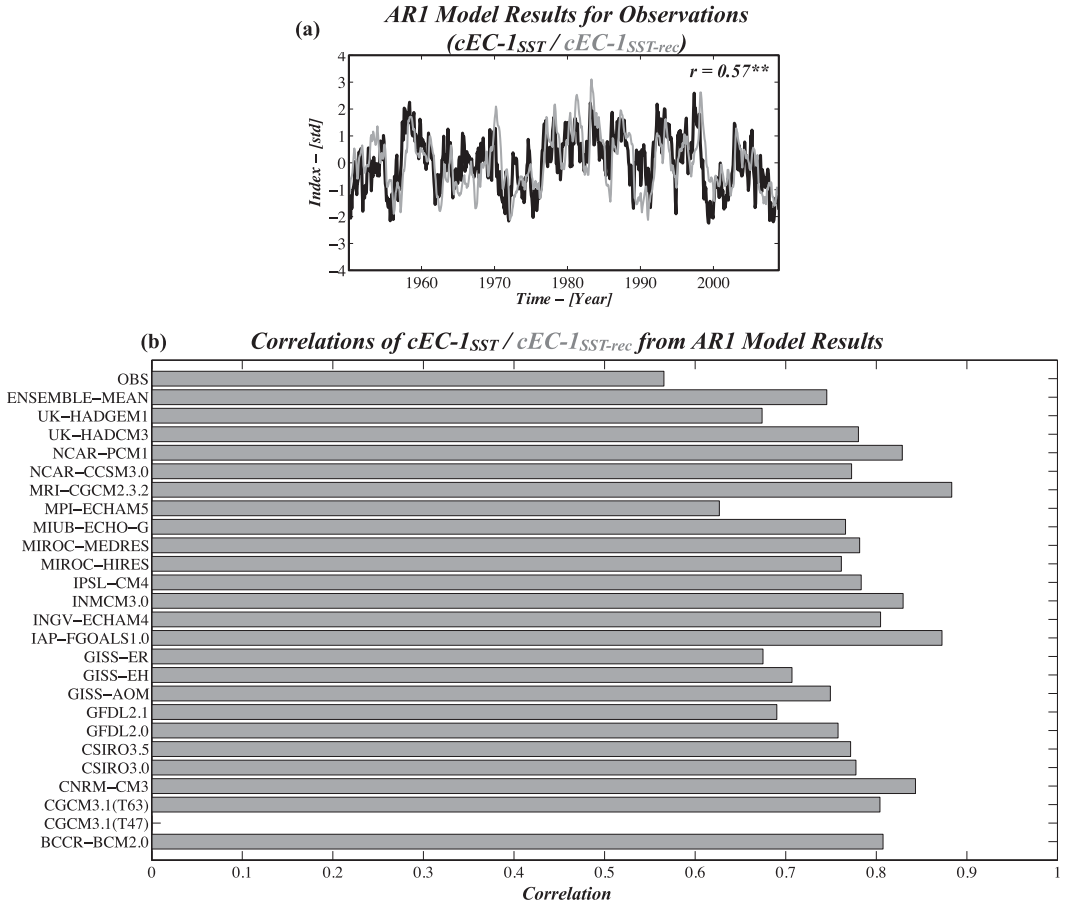

FIG. 6. (a) The observed cEC-1_{SST} index (black line) and the cEC-$l_{SST\text{-}rec}$ index (gray line) from the AR-1 model (see text). Correlation between the cEC-1_{SST} and cEC-$l_{SST\text{-}rec}$ indices is shown and is highly significant ($p < 0.01$; double asterisk). (b) Correlations between the cEC-1_{SST} and cEC-$l_{SST\text{-}rec}$ indices for the observations, the ensemble-mean, and all 24 models for their 20C3M runs. Only correlations exceeding the 95% significance level are plotted.

that the model has less dependency on atmospheric forcing for this mode of variability than observations would suggest. For later lags, the ensemble-mean ACF of the cEC-2_{SST} index continually decays slowly yet still exponentially toward 0 and remains close to 0 at later lags, while the observed ACF of the cEC-2_{SST} index rebounds toward positive correlations after a lag of 10 years (Fig. 8b). The individual models have a more complicated structure, however, with most of them showing positive (and negative) correlations extending out past 10–15-yr lags. Indeed, the ensemble-mean ACF at large lags reflects the spread in positive and negative correlations there, resulting in an ensemble-mean ACF that hovers near 0.

In summary, the AR-1 model results suggest that the models are strongly influenced by the AL in driving their leading SSTa covariability pattern but are less dependent on atmospheric forcing for their second leading SSTa covariability mode. Both of these results are somewhat contrary to the observational results and thus suggest issues with the ways the ocean components of the models integrate forcing from the overlying North Pacific atmosphere.

5. Connections between tropical Pacific climate variability and NPDV in the models

a. Observational evidence

The previous two sections evaluated how extratropical variability of the atmosphere and ocean affect NPDV representation in the IPCC models. We now shift focus to examining how the models capture the relationship between tropical Pacific climate variability and NPDV. This link is important because a significant fraction of variability in NPDV can be explained from tropical Pacific oceanic and atmospheric variability (e.g., Alexander et al. 2002; Deser et al. 2004; Schneider and

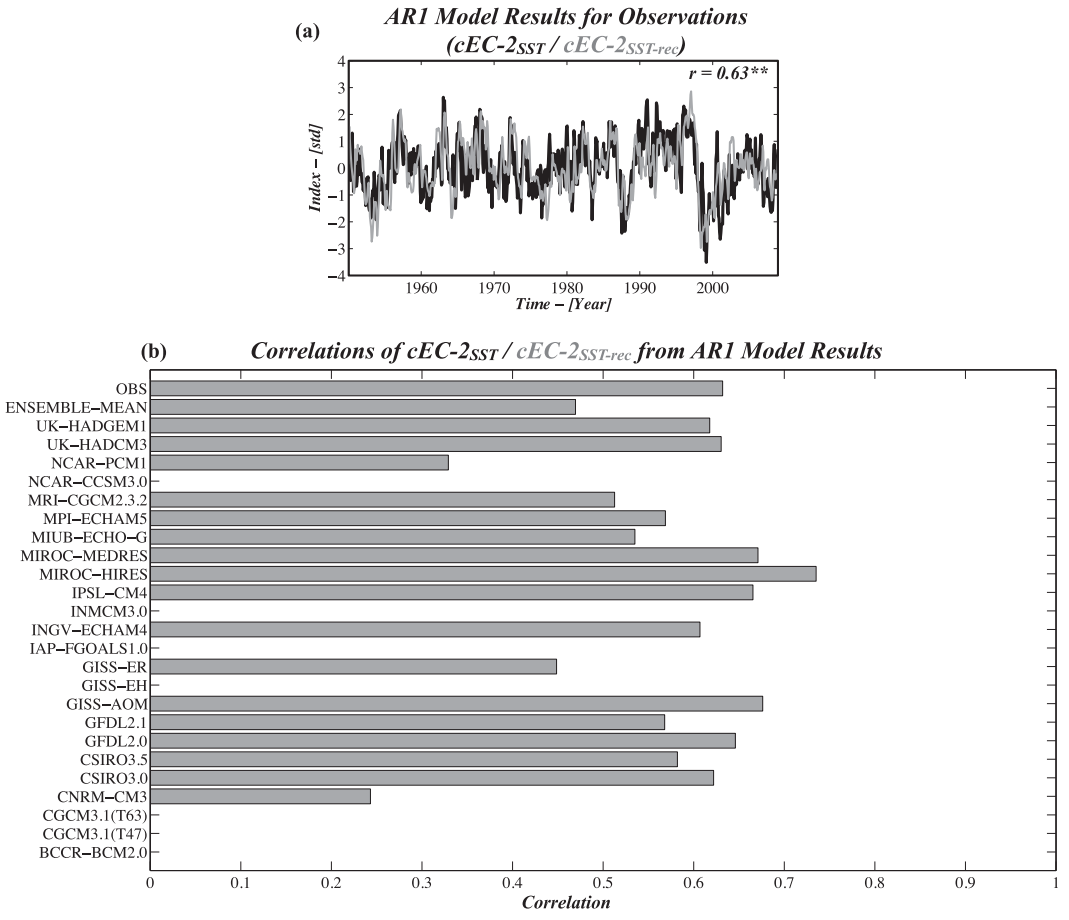

FIG. 7. As in Fig. 6, but for cEC-2_{SST} and cEC-$2_{SST\text{-}rec}$.

Cornuelle 2005; Alexander et al. 2008; Di Lorenzo et al. 2010). These links are primarily established by an atmospheric bridge whereby changes in the Hadley cell and the location and intensity of tropical convection are teleconnected to the midlatitude atmosphere and ocean. For example, canonical ENSO activity projects onto the variability of the AL and is integrated by the ocean, providing a mechanism that drives the PDO (e.g., Alexander et al. 2002; Newman et al. 2003). Recently, another link between North Pacific climate variability and tropical Pacific SSTa has been identified through CPW events (e.g., Ashok et al. 2007), defined as the second leading mode of tropical Pacific SSTa. CPW events have their maximum warming in the central tropical Pacific instead of the eastern tropical Pacific Ocean as during traditional ENSO events and consequently excite unique teleconnection patterns in the Northern Hemisphere in precipitation and SLP (Weng et al. 2009). Like the ENSO–PDO connection, the CPW phenomenon influences low frequency variability of the NPGO (Di Lorenzo et al. 2010).

Given that the characteristics of NPDV in the short observational record are strongly connected dynamically to tropical variability, we implement a simple analysis to extract the statistical signature of the links between canonical ENSO and CPW variability and the patterns of NPDV to test in the climate models. Figure 9 shows the regressions of wintertime SLPa and SSTa on the EC-$l_{tropics\text{-}SST}$ and EC-$2_{tropics\text{-}SST}$ indices (calculated from projection of monthly tropical Pacific SSTa onto EOF-$l_{tropics\text{-}SST}$ and EOF-$2_{tropics\text{-}SST}$, respectively). The thick gray line in all plots denotes where correlations are significant ($p < 0.05$). The SLPa regression pattern with the EC-$l_{tropics\text{-}SST}$ index (Fig. 9a) displays the east–west dipole of negative–positive SLPa indicative of changes in the Walker circulation during warm ENSO events. Moreover, negative anomalies exist in the AL region (cf. the North Pacific sector of Fig. 9a with Fig. 4a). Almost the entire North Pacific and tropical Pacific basin (minus a section through the central portion) exhibit significant correlations with the leading mode of tropical Pacific SSTa.

TABLE 4. Values of τ (months) for the AR-1 model reconstructions for each model and the observations.

Model Name (data)	$\tau_{cEC\text{-}1}$ (months)	$\tau_{csEC\text{-}2}$ (months)
BCCR-BCM2.0	6.2	15.7
CGCM3.1 (T47)	11.2	15.6
CGCM3.1 (T63)	6.7	19.8
CNRM-CM3	6.3	9.7
CSIRO3.0	5.3	7.2
CSIRO3.5	7.4	6.7a
GFDL CM2.0	8.5	7.4
GFDL CM2.1	6.6	7.0
GISS-AOM	3.1	3.9
GISS-EH	5.2	17.7
GISS-ER	4.4	6.8
IAP FGOALS-g1.0	8.3	12.4
INGV ECHAM4	5.7	5.7
INM-CM3.0	6.5	11.5
IPSL CM4	7.2	5.0
MIROC(hires)	4.1	3.2
MIROC(medres)	6.2	5.4
MIUBECHOG	6.2	8.9
MPI ECHAM5	6.3	8.6
MRI CGCM2.3.2	5.1	6.7
NCAR CCSM3.0	7.8	7.2
NCAR PCM1	3.5	4.8
UKMO HadCM3	6.1	8.0
UKMO HadGEM1	4.0	6.5
Ensemble mean	6.2	8.8
Observations	10.2	5.8

In the SSTa regression field (Fig. 9b), the canonical ENSO pattern is visible in the equatorial Pacific. In the North Pacific, the SSTa regression pattern has spatial characteristics similar to EOF-1_{SST} (Fig. la) and cEOF-1_{SST} (Fig. 4b). Together, these two figures are consistent with previous studies showing that the leading mode of tropical Pacific SSTa impacts the leading modes of SLPa and SSTa in the North Pacific. Indeed, the correlation between the EC-$1_{tropics\text{-}SST}$ index and the EC-1_{SST} index is 0.56, which is highly significant ($p < 0.01$).

Figures 9c and 9d illustrate the relationship between the EC-$2_{tropics\text{-}SST}$ index and SLPa and SSTa in the Pacific basin. For SLPa (Fig. 9c), a dipole in the North Pacific exists and closely resembles the NPO-like pattern in Fig. 4c. The positive and significant anomalies across Alaska extend into central North America, which coincides with the baroclinic expression of the NPO on North American weather (Linkin and Nigam 2008). For the SSTa field (Fig. 9d), the regression pattern in the North Pacific resembles cEOF-2_{SST} (Fig. 4d). When comparing the EC-$2_{tropics\text{-}SST}$ and cEC-2_{SST} indices, the correlation is $r = 0.38$, which is significant ($p < 0.01$) but not high. In the tropical Pacific, positive SSTa extend from the subtropical North Pacific into the central and central-western tropical Pacific Ocean, with opposing negative anomalies in the far eastern tropical Pacific. Significance is restricted to the subtropical North Pacific and tropical Pacific features of the pattern.

b. *Model representation of tropical Pacific–North Pacific teleconnections*

The same analysis presented in section 5a is repeated for the 20C3M runs of the models, and the ensemble-mean regression patterns are displayed in Fig. 10. The ensemble-mean SLPa regression pattern associated with the leading mode of tropical Pacific SSTa in the models (Fig. 10a) displays the east–west dipole in SLPa across the tropical Pacific, although at a weaker scale (note the different color bars between Figs. 9 and 10). In the North Pacific, the SLPa pattern matches closely with its

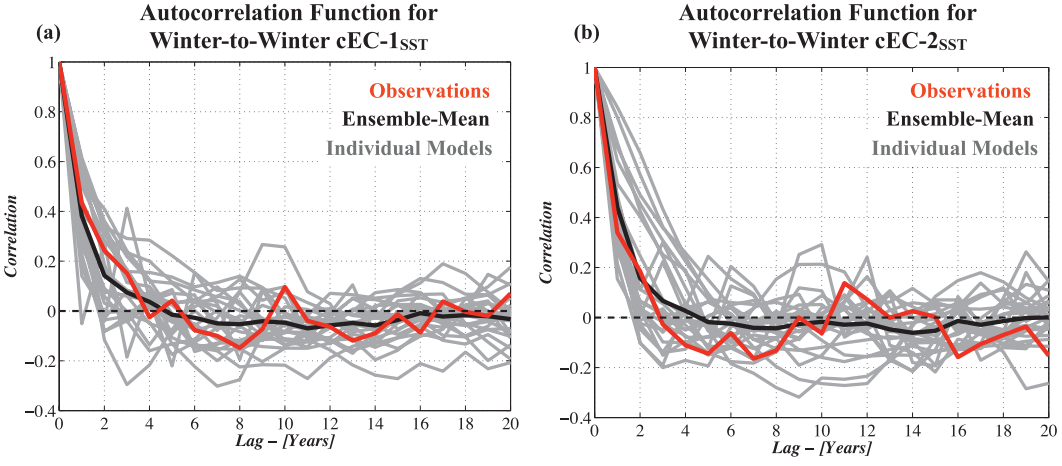

FIG. 8. (a) The winter-to-winter autocorrelation function (lags in years) of the cEC-1_{SST} index for the observations (red), ensemble-mean (black), and the 24 individual models (gray lines). (b) As in (a), but for the cEC-2_{SST} index. Dashed horizontal black line indicates $r = 0$.

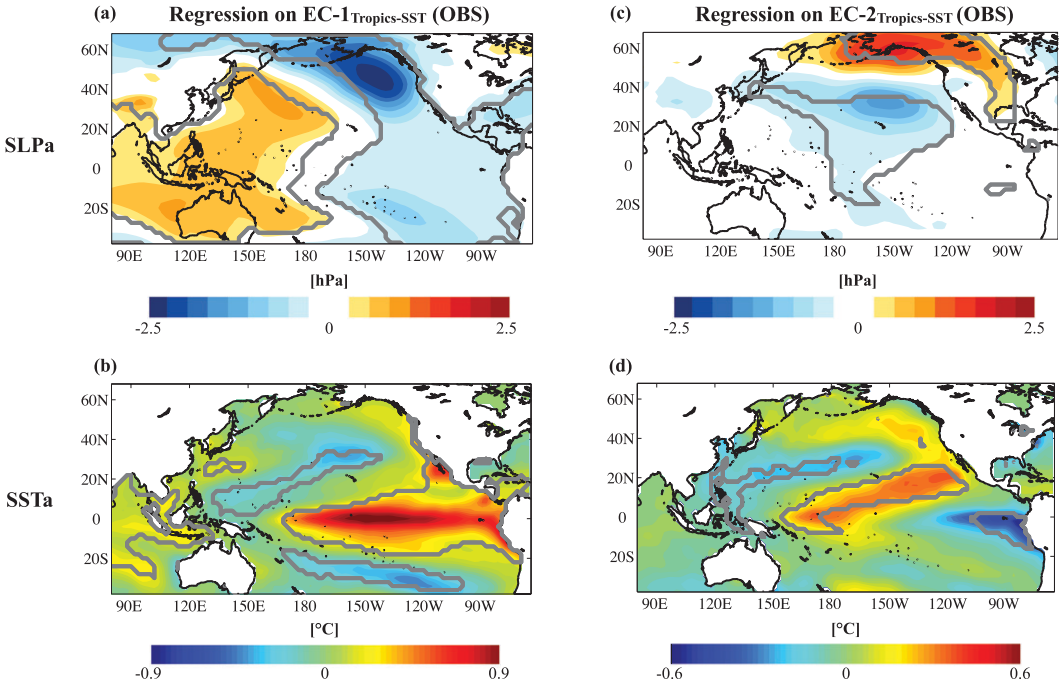

FIG. 9. (a) Regression of observed DJF SLPa (hPa) on the standardized EC-$l_{tropics\text{-}SST}$ index. Thick gray line outlines the region where correlation coefficients exceed the 95% significance level. (b) As in (a), but for DJF SSTa (°C). (c) Regression of observed DJF SLPa (hPa) on the standardized EC-$2_{tropics\text{-}SST}$ index. Thick gray line as in (a). (d) As in (c), but for DJF SSTa (°C).

observational counterpart (Figs. 9a and 10a). However, unlike the observations, this North Pacific signal does not project onto the mean location of the AL in the models (see Fig. 5a). Moreover, the SLPa in the North Pacific sector is void of significant correlations throughout the basin. This lack of significant correlations in the ensemble-mean pattern is related to the differences among the models in the placement and magnitude of the North Pacific SLPa response. In the SSTa field (Fig. 10b), the canonical ENSO pattern is present in the tropical Pacific Ocean though in a much narrower band than in the observations. However, the North Pacific SSTa has no coherent regression pattern and thus no significant correlations. Hence, Figs. 10a and 10b indicate that the IPCC models generally have little dependence between their leading mode of tropical Pacific SSTa variability and North Pacific climate variability—a finding that echoes previous results by Newman (2007).

The ensemble-mean regression patterns of SLPa and SSTa with the EC-$2_{tropics\text{-}SST}$ index are shown in Figs. 10c and 10d, respectively. The SLPa regression pattern (Fig. 10c) has substantial differences in structure in the North Pacific from observations. The SLPa pattern shows a broad region of negative anomalies throughout the central North Pacific with positive anomalies across northwest Canada and Alaska. This pattern is in stark contrast to the NPO-like pattern seen in Fig. 9c and its North American signature. Almost no area in the Pacific basin has significant correlations in the SLPa field, again reflecting the lack of consistency among the different models for the atmospheric response to EOF-$2_{tropics\text{-}SST}$. The ensemble-mean SSTa regression pattern shows the core of tropical Pacific warming displaced into the warm-pool region. Moreover, in the North Pacific, the SSTa regression pattern displays a pattern that resembles more the ensemble-mean EOF-1_{SST} pattern than the ensemble-mean EOF-2_{SST} or cEOF-2_{SST} structures (Figs. 1d and 5d). This difference suggests that variability associated with the leading mode of North Pacific SSTa may have important connections with the *second* leading mode of tropical Pacific SSTa in the models.

To further explore the relationships between the two leading tropical Pacific SSTa modes and the leading mode of variability in the North Pacific, Table 5 shows the correlation between the EC-$l_{tropics\text{-}SST}$ and EC-$2_{tropics\text{-}SST}$ indices with the EC-1_{SST} index in the models. Column 2 of Table 5 shows the correlation between the EC-$l_{tropics\text{-}SST}$ index and the EC-1_{SST} index. In observations, the two indices are significantly correlated ($r = 0.56$; $p < 0.05$). Only one model (the CSIRO3.5 model)

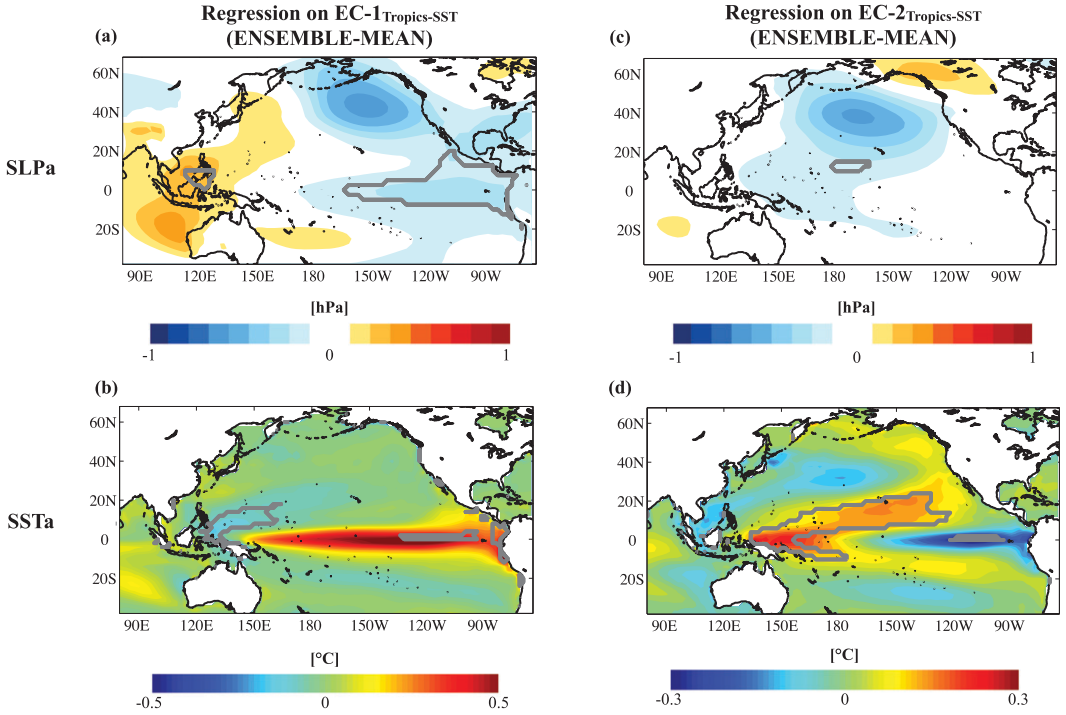

FIG. 10. (a) Ensemble-mean regression pattern of DJF SLPa (hPa) on the standardized EC-$1_{\text{tropics-SST}}$ index. Thick gray line outlines the region where correlation coefficients exceed ±0.2. (b) As in (a), but for DJF SSTa (°C). (c) Ensemble-mean regression pattern of DJF SLPa (hPa) on the standardized EC-$2_{\text{tropics-SST}}$ index; thick gray line is as in (a). (d) As in (c), but for DJF SSTa (°C).

has a correlation nearly that high ($r = 0.60$). Of the remaining models, only seven models have significant ($p < 0.05$) correlations between their EC-$1_{\text{tropics-SST}}$ and EC-1_{SST} indices. By contrast, five models [the BCCR-BCM2.0, the CGCM3.1 (T63), and the three GISS models] display almost zero correlation between the two indices. The mean correlation in the models between the EC-$1_{\text{tropics-SST}}$ and EC-1_{SST} indices is 0.25, which is well below that in observations. By contrast, the correlation between the EC-$2_{\text{tropics-SST}}$ and EC-1_{SST} indices in observations is small and insignificant ($r = 0.17$). However, nine of the 24 models show significant correlations between their EC-$2_{\text{tropics-SST}}$ and EC-1_{SST} indices, with significant correlations ranging from $r = 0.21$ for the CSIRO3.5 model to $r = 0.69$ for the third climate configuration of the Met Office (UKMO) Unified Model (HadCM3). The ensemble-mean correlation for the models is 0.28, which is close to the ensemble-mean correlation between the EC-$1_{\text{tropics-SST}}$ and EC-1_{SST} indices.

6. Discussion and conclusions

Characterizing NPDV in coupled climate models and their predictability skill for short-term and long-term climate are critical research questions in climate dynamics today. Accurately representing in the models the two leading patterns of oceanic and atmospheric variability in the region is integral to answering these questions, as these modes have profound effects on sensible weather downstream through teleconnections and on biological and ocean properties important to coastal ecosystems in the North Pacific. Moreover, both modes are important at decadal time scales, meaning their representation in the models is important for future climate change studies. Most previous studies have looked at characterizing changes in the North Pacific or in the ENSO phenomenon in climate models in isolation from each other. This study complements those studies and goes further by exploring both North Pacific and tropical Pacific climate variability of the IPCC AR4 models when evaluating NPDV. Moreover, we include every realization from each model, in the 20C3M and SRES A1B scenarios, providing a comprehensive examination of NPDV in the coupled climate models.

When testing North Pacific-only variables, the models reliably reproduce the two leading oceanic patterns of variability with high spatial similarity to their observational counterparts (Figs. 1 and 2). Yet, the frequency of those patterns does not agree among the models. For

TABLE 5. Correlations between tropical and North Pacific SST indices for the IPCC models and observations. Correlations exceeding the 95% significance level are in bold.

Model (data)	r(EC-$1_{tropics\text{-}SST}$, EC-1_{SST})	r(EC-$2_{tropics\text{-}SST}$, EC-1_{SST})
BCCR-BCM2.0	0.07	**0.43**
CGCM3.1 (T47)	0.26	0.15
CGCM3.1 (T63)	0.04	0.12
CNRM-CM3	0.15	**0.66**
CSIRO3.0	0.25	**0.32**
CSIRO3.5	**0.60**	**0.21**
GFDL CM2.0	0.20	0.13
GFDL CM2.1	0.29	0.11
GISS-AOM	0.03	0.13
GISS-EH	0.04	0.12
GISS-ER	0.09	0.25
IAP FGOALS-g1.0	**0.36**	**0.61**
INGV ECHAM4	0.17	**0.45**
INM-CM3.0	0.22	0.06
IPSL CM4	**0.35**	0.18
MIROC(hires)	**0.44**	**0.34**
MIROC(medres)	**0.41**	0.16
MIUBECHOG	0.22	0.27
MPI ECHAM5	0.30	0.18
MRI CGCM2.3.2	**0.38**	**0.57**
NCAR CCSM3.0	0.11	0.21
NCAR PCM1	**0.30**	0.20
UKMO HadCM3	**0.37**	**0.69**
UKMO HadGEM1	0.29	0.14
Ensemble mean	0.25	0.28
Observations	**0.56**	0.17

the first SSTa mode (EC-1_{SST}), every model shows the strongest power at the decadal time scales (Fig. 3a), but the total variance in the model indices is less than observed (Table 3, column 2). For the EC-2_{SST} index, however, all models have their strongest power in the 10–20-yr band, while the observations have a dual-peak signature with local maxima at about 5 and 10 years. Another general issue with the models is that their EC-2_{SST} indices exhibit much more variance than observed (Table 3, column 3). This higher-than-observed variance, along with different spectral characteristics of the index, lowers confidence in the predictability of NPDV and even global climate change based on these models.

For implications on future climate change, the coupled climate models show no consensus on projected future changes in the frequency of either the first or second leading pattern of North Pacific SSTa. Neither the difference in power spectra (not shown) nor changes in variances of the indices (Table 3) displays consistent changes between the twentieth and twenty-first centuries in the models. The lack of a consensus in changes in either mode also affects confidence in projected changes in the overlying atmospheric circulation. Work by Bengtsson et al. (2006), Teng et al. (2008), and Ulbrich et al. (2008) suggest that global climate change will influence changes in storm tracks and hence could influence the strength and location of planetary waves and associated climatological features like the AL. Since the wind stress curl induced by the AL and NPO are drivers to the leading modes of North Pacific SSTa, we would expect that changes in their characteristics would change the dominant SSTa patterns. There appears to be a disconnect in this aspect of the models that needs to be addressed.

The results of the AR-1 model test also present more differences between the models and observations in the temporal evolutions of the leading two North Pacific SSTa cEOF patterns. The cEC-1_{SST} index can be reconstructed by forcing the AR-1 model with the atmospheric variability of the AL in both observations and models (Fig. 6), though the correlations between the original and reconstructed indices in the models are much higher than in observations. The cEC-1_{SST} index also appears to have a shorter ''memory'' in the models than observation (Table 4 and Fig. 8a). For the cEC-2_{SST} index (Fig. 7), NPO variability contributes significantly to the index in observations, but the integration of the NPO forcing is more challenging for the models (Fig. 7b). For some models, the NPO does not drive the pattern given by cEOF-2_{SST}. We also find that the memory associated with the second mode is longer in the models than in observations (Table 4), suggesting that the second mode in the models may be tracking an internal ocean mode that is not directly forced by the atmosphere. Indeed, some models that exhibit poor skill in reconstructing the cEC-2_{SST} index (Fig. 7) also perform poorly in reproducing the NPO pattern spatially (cEOF-2_{SLP}; Fig. 2).

Finally, the coupled climate models display very weak or nonexistent links between North Pacific climate variability and the first two dominant modes of tropical Pacific SSTa variability (i.e., ENSO and CPW). The ensemble-mean SSTa and SLPa projections of the two leading modes of tropical Pacific SSTa variability display little to no correlation over the North Pacific, with the midlatitude atmospheric teleconnection having significant differences in amplitude and structure than observed (Figs. 10a and 10b). In the models, both the first and second leading mode of tropical Pacific SSTa project onto PDO-like variability in the North Pacific unlike observations where only the canonical ENSO signature projects significantly onto the AL–PDO mode. In fact, in the ensemble mean, the second mode of tropical Pacific SSTa variability projects onto the SSTa pattern in cEOF-1_{SST}. This inconsistency in the teleconnection may be directly related to the very different structure of the AL between the North Pacific analysis

(Fig. 5a) and the tropical Pacific regression analysis (Fig. 10a). Reasons for this different AL representation remain unclear and may be related to mechanisms associated with the atmospheric bridge, including the distribution of tropical convection in the models, which influences the generation of atmospheric waves that impacts extratropical North Pacific storm tracks.

The relationship between North Pacific variability and the second mode of tropical Pacific SSTa is also not represented well in the coupled models (Figs. 10c and 10d). The North Pacific SLPa pattern associated with EOF-$2_{\text{tropics-SST}}$, in particular, lacks an NPO-like dipole (Fig. 10c). The SSTa regression pattern indicates a ''warm-pool warming'' (Fig. 10d), which is a common issue in select coupled climate models (e.g., Kug et al. 2010). Recent work by Yeh et al. (2009) notes that several of the climate models used in this study forecast significant increases in the frequency of the warm-pool warming El Niño episodes in the SRES A1B scenario. Because of the growing importance of this flavor of ENSO and the inability of the models to capture its relationship with the North Pacific, future work should concentrate on what effects CPW-type ENSO events have dynamically on the midlatitude circulation in observation-based analyses and model experiments.

Another avenue of future research is the role of the NPO in global climate variability. The NPO emerges in both cEOF-2_{SLP} (Fig. 4c) and the regression analysis with the EC-$2_{\text{tropics-SST}}$ index (Fig. 9c). Its forcing on the underlying ocean, the connection with the CPW phenomenon, and with its downstream atmospheric teleconnections suggest that the NPO is important on intraseasonal, interannual, and even on decadal time scales (Di Lorenzo et al. 2010). Recent revival of the NPO in the climate literature in relation to extratropical weather patterns (Linkin and Nigam 2008) and the potential initiation of ENSO events (Vimont et al. 2001, 2003) motivates a focus on potential mechanisms associated with the NPO that can be used to improve its representation in climate models.

This study does not offer definitive evidence of what changes are expected in North Pacific climate variability. The lack of consensus mirrors parallel findings in changes in ENSO behavior conducted by van Oldenborgh et al. (2005), Guilyardi (2006), and Merryfield (2006), for example. Yet, we have identified significant issues with temporal and spatial characteristics of the leading modes of North Pacific variability that most certainly impact global climate change predictions. Even though certain models may appear to perform better than others among the various analyses, the best approach to rectifying future climate change issues likely resides with using multimember ensembles (Reifen and Toumi 2009) for enhancement of the model performance and for predictions.

Acknowledgments. This work was supported by grants from the National Science Foundation for Pacific Boundary and Ecosystems Climate Study (http://www.pobex.org; Grant OCE-0815280) and from the Department of Energy on Pacific Climate Change. The authors would also like to thank three anonymous reviewers for their helpful comments on the manuscript. The authors also acknowledge the various modeling groups for making their simulations available for analysis, as well as the Program for Climate Model Diagnosis and Intercomparison (PCMDI) for collecting and archiving the CMIP3/IPCC AR4 model output.

REFERENCES

Alexander, M. A., C. Deser, and M. S. Timlin, 1999: The reemergence of SST anomalies in the North Pacific Ocean. *J. Climate,* **12,** 2419–2433.

——, I. Bladé, M. Newman, J. R. Lanzante, N.-C. Lau, and J. D. Scott, 2002: The atmospheric bridge: The influence of ENSO teleconnections on air–sea interaction over the global oceans. *J. Climate,* **15,** 2205–2231.

——, L. Matrosova, C. Penland, J. D. Scott, and P. Chang, 2008: Forecasting Pacific SSTs: Linear inverse model predictions of the PDO. *J. Climate,* **21,** 385–402.

Anderson, B. T., 2003: Tropical Pacific sea surface temperatures and preceding sea level pressure anomalies in the subtropical North Pacific. *J. Geophys. Res.,* **108,** 4732, doi:10.1029/2003JD003805.

Ashok, K., S. K. Behera, S. A. Rao, H. Y. Weng, and T. Yamagata, 2007: El Niño Modoki and its possible teleconnection. *J. Geophys. Res.,* **112,** doi:10.1029/2006JC003798.

Bengtsson, L., K. I. Hodges, and E. Roeckner, 2006: Storm tracks and climate change. *J. Climate,* **19,** 3518–3543.

Bond, N. A., J. E. Overland, M. Spillane, and P. Stabeno, 2003: Recent shifts in the state of the North Pacific. *Geophys. Res. Lett.,* **30,** 2183, doi:10.1029/2003GL018597.

Bretherton, C. S., C. Smith, and J. M. Wallace, 1992: An intercomparison of methods for finding coupled patterns in climate data. *J. Climate,* **5,** 541–560.

Ceballos, L., E. Di Lorenzo, N. Schneider, and B. Taguchi, 2009: North Pacific gyre oscillation synchronizes climate fluctuations in the eastern and western North Pacific. *J. Climate,* **22,** 5163–5174.

Chhak, K., E. Di Lorenzo, N. Schneider, and P. Cummins, 2009: Forcing of low-frequency ocean variability in the Northeast Pacific. *J. Climate,* **22,** 1255–1276.

Davis, R. E., 1976: Predictability of sea surface temperature and sea level pressure anomalies over the North Pacific Ocean. *J. Phys. Oceanogr.,* **6,** 249–266.

Deser, C., M. A. Alexander, and M. S. Timlin, 2003: Understanding the persistence of sea surface temperature anomalies in midlatitudes. *J. Climate,* **16,** 57–72.

——, A. S. Phillips, and J. W. Hurrell, 2004: Pacific interdecadal climate variability: Linkages between the tropics and the North Pacific during boreal winter since 1900. *J. Climate,* **17,** 3109–3124.

Di Lorenzo, E., and Coauthors, 2008: North Pacific Gyre Oscillation links ocean climate and ecosystem change. *Geophys. Res. Lett.,* **35,** L08607, doi:10.1029/2007GL032838.

——, and Coauthors, 2009: Nutrient and salinity decadal variations in the central and eastern North Pacific. *Geophys. Res. Lett.,* **36,** L14601, doi:10.1029/2009GL038261.

——, and Coauthors, 2010: Central Pacific El Niño and decadal climate change in the North Pacific. *Nat. Geosci.,* **3,** 762–765.

Graham, N. E., T. P. Barnett, R. Wilde, M. Ponater, and S. Schubert, 1994: On the roles of tropical and midlatitude SSTs in forcing annual to interdecadal variability in the winter Northern Hemisphere circulation. *J. Climate,* **7,** 1416–1442.

Guilyardi, E., 2006: El Niño mean state-seasonal cycle interactions in a multi-model ensemble. *Climate Dyn.,* **26,** 329–348.

Kistler, R., and Coauthors, 2001: The NCEP-NCAR 50-Year Reanalysis: Monthly means CD-ROM and documentation. *Bull. Amer. Meteor. Soc.,* **82,** 247–267.

Kug, J.-S., J. Choi, S.-I. An, F.-F. Jin, and A. T. Wittenberg, 2010: Warm pool and cold tongue El Niño events as simulated by the GFDL 2.1 coupled GCM. *J. Climate,* **23,** 1226–1239.

Latif, M., and T. P. Barnett, 1996: Decadal climate variability over the North Pacific and North America: Dynamics and predictability. *J. Climate,* **9,** 2407–2423.

Linkin, M. E., and S. Nigam, 2008: The North Pacific oscillation–west Pacific teleconnection pattern: Mature-phase structure and winter impacts. *J. Climate,* **21,** 1979–1997.

Mantua, N. J., and S. R. Hare, 2000: The Pacific decadal oscillation. *J. Oceanogr.,* **58,** 35–44.

——, ——, Y. Zhang, J. M. Wallace, and R. Francis, 1997: A Pacific interdecadal climate oscillation with impacts on salmon production. *Bull. Amer. Meteor. Soc.,* **78,** 1069–1079.

McGowan, J. A., S. J. Bograd, R. J. Lynn, and A. J. Miller, 2003: The biological response to the 1977 regime shift in the California Current. *Deep-Sea Res. II,* **50,** 2567–2582.

Meehl, G. A., H. Teng, and G. Branstator, 2006: Future changes of El Niño in two global coupled climate models. *Climate Dyn.,* **26,** 549–566.

Merryfield, W. J., 2006: Changes to ENSO under CO_2 doubling in a multimodel ensemble. *J. Climate,* **19,** 4009–4027.

Miller, A. J., F. Chai, S. Chiba, J. R. Moisan, and D. J. Neilson, 2004: Decadal-scale climate and ecosystem interactions in the North Pacific Ocean. *J. Oceanogr.,* **60,** 163–188.

Namias, J., 1969: Seasonal interactions between the North Pacific Ocean and the atmosphere during the 1960's. *Mon. Wea. Rev.,* **97,** 173–192.

——, 1972: Experiments in objectively predicting some atmospheric and oceanic variables for the winter of 1971–1972. *J. Appl. Meteor.,* **11,** 1164–1174.

Newman, M., 2007: Interannual to decadal predictability of tropical and North Pacific sea surface temperatures. *J. Climate,* **20,** 2333–2356.

——, G. P. Compo, and M. A. Alexander, 2003: ENSO-forced variability of the Pacific decadal oscillation. *J. Climate,* **16,** 3853–3857.

North, G. R., T. L. Bell, R. F. Cahalan, and F. J. Moeng, 1982: Sampling errors in the estimation of empirical orthogonal functions. *Mon. Wea. Rev.,* **110,** 699–706.

Overland, J., and M. Wang, 2007: Future climate of the North Pacific Ocean. *Eos, Trans. Amer. Geophys. Union,* **88,** 178–182.

Pierce, D. W., T. P. Barnett, N. Schneider, R. Saravanan, D. Dommentget, and M. Latif, 2001: The role of ocean dynamics in producing decadal climate variability in the North Pacific. *Climate Dyn.,* **18,** 51–70.

Reifen, C., and R. Toumi, 2009: Climate projections: Past performance no guarantee of future skill? *Geophys. Res. Lett,* **36,** L13704, doi:10.1029/2009GL038082.

Rogers, J. C., 1981: The North Pacific oscillation. *J. Climatol.,* **1,** 39–57.

Schneider, N., and B. D. Cornuelle, 2005: The forcing of the Pacific decadal oscillation. *J. Climate,* **18,** 4355–4373.

Smith, T. M., R. W. Reynolds, T. C. Peterson, and J. Lawrimore, 2008: Improvements to NOAA's historical merged land–ocean surface temperature analysis (1880–2006). *J. Climate,* **21,** 2283–2296.

Teng, H., W. M. Washington, and G. A. Meehl, 2008: Interannual variations and future change of extratropical cyclone activity over North America in CCSM3. *Climate Dyn.,* **30,** 673–686.

Torrence, C., and G. P. Compo, 1998: A practical guide to wavelet analysis. *Bull. Amer. Meteor. Soc.,* **79,** 61–78.

Trenberth, K. E., 1990: Recent observed interdecadal climate changes in the Northern Hemisphere. *Bull. Amer. Meteor. Soc.,* **71,** 988–993.

——, and J. W. Hurrell, 1994: Decadal atmosphere–ocean variations in the Pacific. *Climate Dyn.,* **9,** 1004–1020.

Ulbrich, U., J. G. Pinto, H. Kupfer, C. Leckebusch, T. Spangehl, and M. Reyers, 2008: Changing Northern Hemisphere storm tracks in an ensemble of IPCC climate change simulations. *J. Climate,* **21,** 1669–1679.

van Oldenborgh, G. J., S. Y. Philip, and M. Collins, 2005: El Niño in a changing climate: A multi-model study. *Ocean Sci.,* **1,** 81–95.

Vimont, D. J., D. S. Battisti, and A. C. Hirst, 2001: Footprinting: A seasonal connection between the tropics and mid-latitudes. *Geophys. Res. Lett.,* **28,** 3923–3926.

——, J. M. Wallace, and D. S. Battisti, 2003: The seasonal footprinting mechanism in the Pacific: Implications for ENSO. *J. Climate,* **16,** 2668–2675.

Walker, G. T., and E. W. Bliss, 1932: World weather V. *Mem. Roy. Meteor. Soc.,* **4,** 53–84.

Weng, H. Y., S. K. Behera, and T. Yamagata, 2009: Anomalous winter climate conditions in the Pacific rim during recent El Niño Modoki and El Niño events. *Climate Dyn.,* **32,** 663–674.

Yasuda, I., H. Sugusaki, Y. Watanabe, S. Minobe, and Y. Oozeki, 1999: Interdecadal variations in Japanese sardine and ocean/climate. *Fish. Oceanogr.,* **8,** 18–24.

Yeh, S.-W., and B. P. Kirtman, 2007: ENSO amplitude changes due to climate change projections in different coupled models. *J. Climate,* **20,** 203–217.

——, J.-S. Kug, B. Dewitte, M.-H. Kwon, B. P. Kirtman, and F.-F. Jin, 2009: El Nino in a changing climate. *Nature,* **461,** 511–514.

Zhang, Y., J. M. Wallace, and D. S. Battisti, 1997: ENSO-like interdecadal variability. *J. Climate,* **10,** 1004–1020.